

Dynamics of galaxies and clusters in *refracted gravity*

Titos Matsakos^a and Antonaldo Diaferio^{b,c}

^aDept. of Astronomy & Astrophysics, The University of Chicago, Chicago, IL 60637, USA

^bDipartimento di Fisica, Università di Torino, via P. Giuria 1, 10125, Torino, Italy

^cIstituto Nazionale di Fisica Nucleare (INFN), Sezione di Torino, Torino, Italy

E-mail: titos.matsakos@uchicago.edu, diaferio@ph.unito.it

Abstract. We investigate the proof of concept and the implications of *refracted gravity*, a novel modified gravity aimed to solve the discrepancy between the luminous and the dynamical mass of cosmic structures without resorting to dark matter. Inspired by the behavior of electric fields in matter, refracted gravity introduces a gravitational permittivity that depends on the local mass density and modifies the standard Poisson equation. The resulting gravitational field can become more intense than the Newtonian field and can mimic the presence of dark matter. We show that the refracted gravitational field correctly describes (1) the rotation curves and the Tully-Fisher relation of disk galaxies; and (2) the observed temperature profile of the X-ray gas of galaxy clusters. According to these promising results, we conclude that refracted gravity deserves further investigation.

Keywords: modified gravity, rotation curves of galaxies, galaxy dynamics, galaxy clusters

ArXiv ePrint: ??

Contents

1	Introduction	1
2	The basics of <i>refracted gravity</i>	2
2.1	Elements from electrodynamics	2
2.2	Formulation of <i>refracted gravity</i>	3
2.2.1	Assumptions for the permittivity	3
2.2.2	Flat systems	4
2.2.3	Spherical systems	4
2.3	A simplified RG framework (SRG) for flat systems	5
2.3.1	Quantifying the deviations from the inverse square law	6
2.3.2	Basic implications	7
3	Application of SRG to disk galaxies	8
3.1	Rotation curves	9
3.2	The baryonic Tully-Fisher relation	11
3.3	Mass discrepancies	12
3.4	Velocity dispersions in the Milky Way	13
4	Solving the RG field equation	15
4.1	Application to a model disk galaxy	15
4.2	Rotation curves of NGC1560 and NGC6946	17
4.3	Intracluster gas temperature of A1991 and A1795	18
5	Discussion	19
5.1	Disk scale heights z_0 and h	19
5.2	Relation to dark matter	20
5.3	Relation to MOND	21
6	Other applications	23
6.1	Globular clusters	23
6.2	Dwarf spheroidal galaxies	23
6.3	Elliptical galaxies	24
6.4	Disk galaxies	24
6.5	Galaxy groups and clusters	24
7	Conclusion	25

1 Introduction

It is a well-established fact that visible matter cannot account for the dynamics observed from galactic scales up to cosmological scales when described by General Relativity and its Newtonian weak-field limit. In particular, significant deviations appear in galactic rotation curves, where the velocities of stars indicate an acceleration or gravitational force proportional

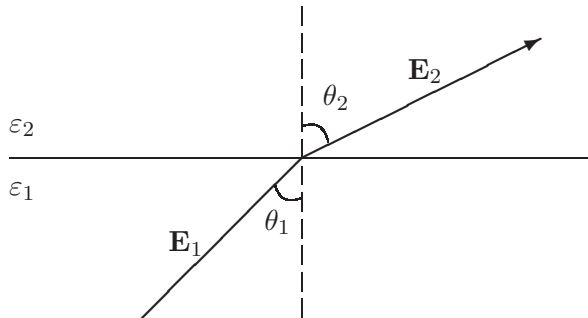


Figure 1. Refraction of an electric field line that threads two media of different permittivities, $\varepsilon_1 < \varepsilon_2$.

to the inverse of the radial distance, r^{-1} , rather than r^{-2} .¹ Moreover, when interpreted in standard gravity, the velocity dispersion of galaxies in clusters, the temperature of the intracluster gas, and gravitational lensing effects, all suggest that the gravitating mass of clusters is five to ten times larger than the mass that emits the electromagnetic radiation. The most widely accepted interpretation of this mass discrepancy is the existence of dark matter (DM) which originates the additional gravitational pull (e.g. [1] for a review).

In this paper we propose a new concept that is inspired by the theory of electrodynamics in matter. In particular, a dielectric medium of a non-uniform permittivity can affect both the direction and magnitude of electric fields. Here, we investigate whether a similar framework could also describe the peculiar behavior of gravity in large-scale systems. We find that the hypothesis of a “refracted gravitational field” can in fact capture many of the observed properties of disk galaxies and galaxy clusters, as well as other objects.

The paper is structured as follows. In section 2 we introduce the concept of *refracted gravity* (RG) and we describe its mathematical formulation. At the end of that section we present a framework that simplifies the calculations, we derive some of its direct implications, and in section 3 we apply it to disk galaxies. In section 4 we solve the full RG equation, apply it to some specific observed disk galaxies and clusters of galaxies, and confront its predictions with several mass-discrepancy observations. In section 5 we compare RG with DM and with MODified Newtonian Dynamics (MOND [2–4], see [5] for a review) and in section 6 we discuss the role of RG in other cosmic systems. Finally, in section 7 we summarize the main points and report possible directions for future work.

2 The basics of *refracted gravity*

2.1 Elements from electrodynamics

In the interior of a dielectric medium with no free charges, the electric field \mathbf{E} obeys the equation:

$$\nabla \cdot (\varepsilon \mathbf{E}) = 0, \quad (2.1)$$

where $\varepsilon \geq 1$ is the electric permittivity. In vacuum, $\varepsilon = 1$ and Poisson’s law is recovered. Equation (2.1) implies that, whenever a field line crosses a surface that separates two media

¹ Hereafter, we will use the terms acceleration and force interchangeably, where force clearly refers to force per unit mass.

with different permittivities, it is refracted according to:

$$\frac{\tan \theta_1}{\tan \theta_2} = \frac{[E_2]_{\perp}}{[E_1]_{\perp}} = \frac{\varepsilon_1}{\varepsilon_2}, \quad (2.2)$$

where the symbol “ \perp ” denotes the component perpendicular to the interface, see figure 1. Note that the magnitude of the electric field is reduced due to polarization effects; specifically, the component parallel to the interface remains unchanged whereas the perpendicular component decreases.

Motivated by electrodynamics, we explore a similar framework for gravity. By introducing a “gravitational permittivity”, a function monotonically dependent on the mass density, we investigate the implications of the refracted gravitational field in galactic systems.

2.2 Formulation of *refracted gravity*

In analogy to electric fields in matter, in RG the gravitational field obeys the following Poisson equation:

$$\nabla \cdot (\epsilon \nabla \Phi) = 4\pi G \rho, \quad (2.3)$$

where ρ is the ordinary matter density, Φ the gravitational potential, and $\epsilon = \epsilon(\rho)$ the gravitational permittivity that depends on the local density. An equation only formally similar to Eq. (2.3) was proposed for MOND in ref. [6]. However, in that case the function ϵ depends on the field, i.e. $\epsilon_{\text{MOND}} = \epsilon(\nabla \Phi)$, rather than on the source as we propose here. This difference is clearly fundamental; we compare the two approaches in detail in section 5.3.

Contrary to electromagnetism, the permittivity of Eq. (2.3) takes the values $0 < \epsilon_0 \leq \epsilon(\rho) \leq 1$, where $\epsilon_0 = \epsilon(0)$ is the permittivity of vacuum. Specifically, it is approximately unity within matter and has a smaller but constant value in vacuum, $\epsilon(0) = \epsilon_0 < 1$.

RG is thus based on two assumptions:

- (1) The field equation for the gravitational potential is given by Eq. (2.3);
- (2) $\epsilon = \epsilon(\rho)$ is a monotonically increasing function of ρ , with $0 < \epsilon_0 \leq \epsilon(\rho) \leq 1$ and $\epsilon_0 = \epsilon(0) < 1$.

The deviations from Newtonian gravity become apparent by considering the inner product of Eq. (2.3):

$$\nabla \cdot (\epsilon \nabla \Phi) = \frac{\partial \epsilon}{\partial \rho} \nabla \rho \cdot \nabla \Phi + \epsilon \nabla^2 \Phi. \quad (2.4)$$

The two relevant modifications to the standard Poisson equation is the additional term $(\partial \epsilon / \partial \rho) \nabla \rho \cdot \nabla \Phi$ and the factor ϵ in front of the Laplacian. If we broadly classify all astronomical objects – from stellar scales up to galaxy clusters – into spherical- and flat-shaped objects, we see that large deviations from standard gravity appear in flat structures due to the redirection of the field lines (first term of the right-hand side in Eq. 2.4), and in spherical systems due to the value of ϵ which effectively amplifies the field at large distances (second term of the right-hand side in Eq. 2.4).

2.2.1 Assumptions for the permittivity

The mass densities in cosmic structures differ by orders of magnitudes from planetary systems to galaxies, galaxy clusters, and large-scale structures. In contrast, the gravitational

permittivity is limited to $\epsilon \in [\epsilon_0, 1]$. We may thus expect that a proper approximation for the permittivity is

$$\epsilon(\rho) \simeq \begin{cases} 1 & \text{for } \rho \gg \rho_c \\ \epsilon_0 & \text{for } \rho \ll \rho_c \end{cases}, \quad (2.5)$$

where ρ_c is some critical density.

More generally, we note that the permittivity $\epsilon(\rho)$ could in principle depend on other local variables that characterize the gravitational sources, such as the energy density or the entropy. As long as any such quantity exhibits contours similar to ρ , then the corresponding phenomenology would be in agreement with all the observational tests discussed in sections 3 and 4 below. Here, we only consider ρ because it is the simplest hypothesis.

Furthermore, by introducing the permittivity ϵ as a function of density ρ , we unavoidably introduce a smoothing length D over which we average the density field. We limit the present analysis to a proof of concept and postpone the investigation of this crucial topic to future work; here, we simply speculate that the scale of D is expected to be of astronomical interest, for example tens of astronomical units or larger, because the mass discrepancy problem appears to be relevant on scales larger than the solar system. A number of additional serious issues remain open, including a possible incompatibility with special relativity due to the introduction of the vacuum permittivity or a possible violation of the Strong Equivalence Principle. The consequences of a variational approach applied to a possible RG Lagrangian of the form

$$L = \frac{\epsilon}{8\pi G} (\nabla\Phi)^2 + \rho\Phi \quad (2.6)$$

should also be investigated. However, in this paper we limit our study to assess whether this new idea appears promising, at least phenomenologically. If so, we will explore all these fundamental issues elsewhere.

2.2.2 Flat systems

Flat systems have a strong vertical density stratification and hence the value of ρ_c is reached at a given height. As explained in the following sections, Eq. (2.3) suggests that in such objects the field is redirected and, near the disk, it becomes almost parallel to the density layers.

To estimate the effect of this reorientation of the field lines on the exerted force, consider the following example. The directions of the field lines originating from a point source are uniformly distributed over a solid angle of 4π sr. Consequently, the conservation of the field flux implies that the field strength drops proportionally to the inverse of the spherical surface, $4\pi R^2$. Now consider a mechanism that redirects the field lines at large distances parallelly to a specific plane. In this case, the conservation of flux implies a power law for the field that is proportional to the inverse of the circular circumference, namely $\propto r^{-1}$. As it is shown in sections 2.3.1 and 3, this is the main mechanism in RG that changes the radial profile of the acceleration within a disk galaxy from $\propto r^{-2}$ close to its center to $\propto r^{-1}$ farther out.

2.2.3 Spherical systems

If in the central regions of a spherical system, such as a galaxy cluster, the density is larger than the critical value, $\rho > \rho_c$, then the permittivity is unity, $\epsilon = 1$, and hence the field is given by the standard Poisson equation:

$$\nabla^2\Phi = 4\pi G\rho. \quad (2.7)$$

In this case no deviations from Newtonian gravity are expected in RG. On the contrary, in the outer regions where the density eventually drops below the critical value ρ_c , the permittivity becomes $\epsilon = \epsilon_0 < 1$. Due to the spherical symmetry $\nabla\rho$ and $\nabla\Phi$ are parallel and hence the field lines remain radial (see Eq. 2.4). Nevertheless, the strength of the field deviates from the Newtonian law and appears stronger:

$$\nabla^2\Phi = 4\pi G \frac{\rho}{\epsilon_0}. \quad (2.8)$$

In principle, measurements of the dynamical properties of spherical systems – namely stars and globular clusters that exhibit a Newtonian behavior, and elliptical galaxies and galaxy clusters that show increasing departure from Newtonian dynamics – can be used to estimate the values of ρ_c and ϵ_0 .

2.3 A simplified RG framework (SRG) for flat systems

In order to solve Eq. (2.3), an explicit expression is required for $\epsilon(\rho)$ with specific values for ϵ_0 and ρ_c . We undertake this task in section 4. Here, we refrain from exploring special cases given by specific permittivity expressions, and adopt a simplified but general approach to highlight the basic properties of the theory. For spherical systems we may employ Eq. (2.8) to infer the phenomenology in regions where $\rho < \rho_c$: it follows that the SRG field is equivalent to the Newtonian gravitational field of an effective mass distribution $\rho/\epsilon_0 > \rho$ (see also section 5.2). However, such an approach cannot apply to flat systems because it does not account for the redirection of the field lines. Instead, we may approximate Eq. (2.5) with a two-valued permittivity $\epsilon \in \{0, 1\}$ and assume that the transition is defined by the threshold ρ_c . Even though we consider for simplicity $\epsilon_0 = 0$, we note that the redirection of the field lines takes place for any value less than unity; the smaller the value of the vacuum permittivity the stronger is the effect. For $\epsilon_0 = 0$ we may estimate the gravitational field in the region $\epsilon = 1$ by applying the following condition on the iso-surface of ρ_c :

$$\nabla_{\perp}\Phi \simeq 0. \quad (2.9)$$

These approximations to Eq. (2.3) are equivalent to solving the standard Newtonian Poisson equation with the boundary condition of Eq. (2.9) on the density contour $\rho = \rho_c$.² Due to the vertical density stratification of flat objects, such as disk galaxies, we may approximate the iso-surface of ρ_c as two parallel planes above and below the disk. In turn, the boundary condition at that height, e.g. $z = \pm h$, provides the mechanism to redirect all the field flux within the volume defined by $-h \leq z \leq h$. This effect entails from Eq. (2.9), which represents a reflective boundary condition: it reverses the sign of the perpendicular component of the gradient whereas it keeps the parallel component unchanged. In section 4 we show that this approach is indeed a valid approximation by comparing it with the numerical solution of the full RG field equation.

SRG essentially introduces the parameter h to determine the volume surrounding flat systems within which the gravitational flux is redirected. In the central regions, i.e. on scales

² The equivalence becomes evident when Eq. (2.3) is associated to a time-dependent equation of a similar form, such as the heat equation, $\partial T/\partial t = \nabla \cdot (k\nabla T)$. For a given time interval, an interface that separates two media with (T_1, k_1) and (T_2, k_2) behaves as an insulator when $k_1 = 1$ and $k_2 \rightarrow 0$, i.e. $[\nabla T_1]_{\perp} \simeq 0$. Analogously, in the limit $k_2 \rightarrow 0$ the characteristic time scale of heat transfer in region 2 becomes infinite, and thus the steady-state temperature distribution in region 1 can be effectively described by a Poisson equation with a zero-flux boundary condition.

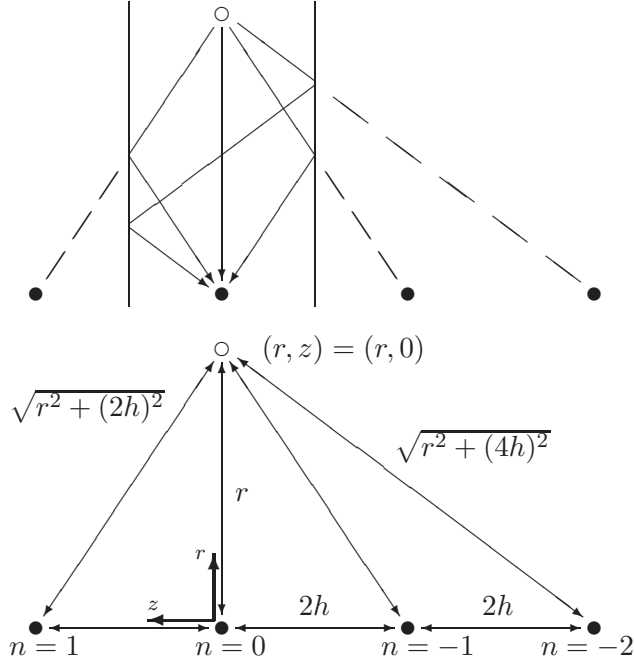


Figure 2. Top panel: a point mass between reflective boundaries (second solid circle from the left) is equivalent to a chain of equally spaced and aligned point masses. The open circle represents a test particle. Bottom panel: the configuration from which Eq. (2.10) is derived.

much smaller than h , field-redirection effects are negligible. Conversely, strong deviations from the Newtonian regime are expected in the outskirts of such objects. With this general approach we may perform explicit calculations to describe the approximate topology of the field given by Eq. (2.3) for any expression of ϵ that obeys Eq. (2.5).

2.3.1 Quantifying the deviations from the inverse square law

In order to quantify the effects of SRG, we assume that the disk galaxy is a point mass m in between a bounding surface of two infinite parallel planes whose separation is equal to $2h$. As shown in the top panel of figure 2, the reflective property of the boundary condition (Eq. 2.9) makes the system equivalent to a chain of infinite, aligned, and equally-spaced point masses in the Newtonian framework (bottom panel). By setting an integer label n for each node of mass m , with $n = 0$ corresponding to the reference mass, the distance between the nodes $n = 0$ and $n = k$ is equal to $2kh$.

In cylindrical coordinates, where the z axis is taken along the chain of masses, it is straightforward to derive the force at distance r from the reference node:

$$F(r, 0) = - \sum_{n=-\infty}^{\infty} \left[\frac{Gm}{r^2 + (2nh)^2} \frac{r}{\sqrt{r^2 + (2nh)^2}} \right] = -\frac{Gm}{r^2} - 2 \sum_{n=1}^{\infty} \frac{Gmr}{[r^2 + (2nh)^2]^{3/2}}. \quad (2.10)$$

For $r \ll h$ the first term dominates and the inverse square law is recovered, i.e. $F \simeq -Gm/r^2$. To the first order correction, we have

$$F(r) \simeq -\frac{Gm}{r^2} - \frac{Gmr}{4h^3} \sum_{n=1}^{\infty} \frac{1}{n^3} = -\frac{Gm}{r^2} - \frac{Gmr}{4h^3} \zeta(3), \quad (2.11)$$

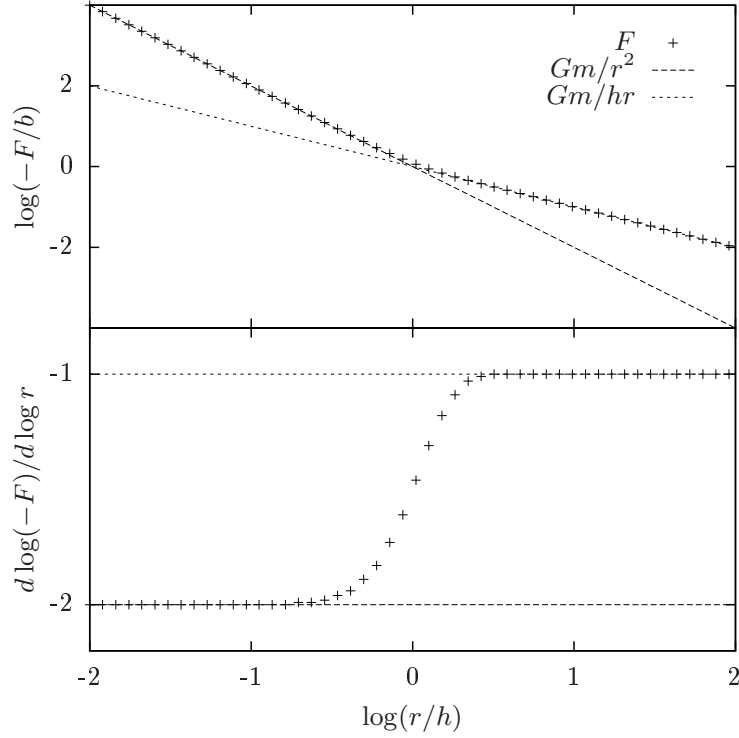


Figure 3. Top panel: radial profile of the force generated by a point mass in between two reflective parallel planes (Eq. 2.10). Bottom panel: the effective radial exponent of Eq. (2.10). For small radii, $r \ll h$, F is proportional to r^{-2} , while for large ones, $r \gg h$, the power law becomes $F \propto r^{-1}$.

where $\zeta(q) = \sum_{n=1}^{\infty} n^{-q}$ is the Riemann zeta function, and $\zeta(3) \simeq 1.2$. In the other limit, $r \gg h$, the force becomes $F \simeq -Gm/hr$. In fact the Newtonian gravitational field of a continuous massive string with linear density $m/2h$ exactly is $F = -Gm/hr$, an elementary application of the Gauss theorem; in RG, the effect of representing the massive point source as a continuous massive string only appears evident at large distances $r \gg h$.

In order to visualize the profile of Eq. (2.10), the top panel of figure 3 plots its values normalized to the acceleration

$$b = \frac{Gm}{h^2} \quad (2.12)$$

as a function of the distance normalized to h . The bottom panel shows the corresponding index of the power law at each location. The change in the radial dependence occurs at the region where r is of the order of h , around which the force switches from $F \propto r^{-2}$ to $F \propto r^{-1}$.

2.3.2 Basic implications

Focusing on the plane $z = 0$, the Newtonian force is $N = -Gm/r^2$ and the orbital velocity at distance r is $v_N = \sqrt{-Nr}$. For $r \ll h$ the Keplerian rotation is recovered, i.e. $F \simeq N$ and thus $v_F \simeq v_N = \sqrt{Gm/r}$. However, for $r \gg h$ the orbital velocity in the presence of F becomes

$$v_F = \sqrt{-Fr} \simeq \sqrt{\frac{Gm}{h}} = v_f. \quad (2.13)$$

Notably, this asymptotic value does not depend on r : the velocity v_f has a flat rotation profile which is denoted with the subscript “f”.

Moreover, the elimination of h from Eq. (2.13) (using Eq. 2.12) gives:

$$v_f^4 = Gbm. \quad (2.14)$$

By assuming a constant mass-to-light ratio, Eq. (2.14) reproduces the slope of the empirical Tully-Fisher relation [7]. To be also consistent with the observed normalization of the Tully-Fisher relation, b must be the constant

$$b \simeq 1.2 \cdot 10^{-10} \text{ m s}^{-2}, \quad (2.15)$$

as shown in ref. [5]. The combination of Eqs. (2.13) and (2.14) links the location of the parallel plane boundaries to the total mass, i.e. $h = \sqrt{Gm/b}$. In the case of disk galaxies the parameter h can be related to the scale height of the disk, as it is argued in section 5.1 below.

Furthermore, the ratio of the squared velocities of the RG and Newtonian fields, termed mass discrepancy [8], is equal to $(v_F/v_N)^2 = F/N$. For r smaller than h the fraction is unity, whereas in the other limit, $r \gg h$, it becomes

$$\frac{v_F^2}{v_N^2} = \frac{F}{N} \simeq \frac{Gm/hr}{Gm/r^2} = \frac{r}{h}. \quad (2.16)$$

In this region it is straightforward to rewrite the above relation as a function of the forces, F or N :

$$\frac{v_F^2}{v_N^2} \simeq \frac{b}{-F}, \quad (2.17)$$

$$\frac{v_F^2}{v_N^2} \simeq \sqrt{\frac{b}{-N}}. \quad (2.18)$$

These expressions match well the observed profiles [5, 8], see section 3.3.

3 Application of SRG to disk galaxies

The stellar distribution of a disk galaxy can be roughly approximated as a thin disk of surface density $\sigma(r) = \sigma_0 \exp(-r/r_0)$, where σ_0 and r_0 are constants [9]. For the sake of simplicity the bulge and the gas components are neglected in the following estimates. The Newtonian gravitational potential in cylindrical coordinates, with the origin located at the center of the disk, is

$$\Phi_N(r, z) = - \int_0^{2\pi} \int_0^\infty \frac{G\sigma_0 e^{-r'/r_0} r' dr' d\phi}{\sqrt{r'^2 - 2rr' \cos \phi + r^2 + z^2}}, \quad (3.1)$$

and the total enclosed mass is

$$m = \int_0^{2\pi} \int_0^\infty \sigma_0 e^{-r'/r_0} r' dr' d\phi = 2\pi\sigma_0 r_0^2. \quad (3.2)$$

Following the SRG approach, we consider the iso-surface of ρ_c to consist of two parallel planes – located at $\pm h$ above and below the disk – and we assume that $\nabla_\perp \Phi = 0$ holds on

Name	$\sigma_0 [M_\odot \text{ pc}^{-2}]$	$r_0 [\text{kpc}]$	$m [M_\odot]$	$h [\text{kpc}]$
G0	$2.4 \cdot 10^2$	3.3	$1.7 \cdot 10^{10}$	4.4
G1	$9.6 \cdot 10^2$	1.5	$1.4 \cdot 10^{10}$	4.0
G2	$2.4 \cdot 10^3$	3.3	$1.7 \cdot 10^{11}$	14
G3	$9.6 \cdot 10^2$	7.6	$3.5 \cdot 10^{11}$	20
G4	$2.4 \cdot 10^2$	10	$1.5 \cdot 10^{11}$	13
G5	$5.7 \cdot 10^1$	7.6	$2.1 \cdot 10^{10}$	5.0
G6	$2.4 \cdot 10^1$	3.3	$1.7 \cdot 10^9$	1.4
G7	$5.7 \cdot 10^1$	1.5	$8.6 \cdot 10^8$	1.0
G8	$2.4 \cdot 10^2$	1.0	$1.5 \cdot 10^9$	1.3
M1	$4.8 \cdot 10^3$	5.0	$7.7 \cdot 10^{11}$	30
M2	$1.5 \cdot 10^3$	9.0	$7.8 \cdot 10^{11}$	30
M3	$4.8 \cdot 10^2$	16	$7.8 \cdot 10^{11}$	30

Table 1. Disk galaxy models with typical values for σ_0 , r_0 , m , and h . They are shown with open circles (G0–G8) and open squares (M1–M3) in figure 4.

this boundary. The system is equivalent to a sequence of infinite and parallelly aligned disks of surface density $\sigma(r)$, similarly to figure 2. In this context, the potential is

$$\Phi_F(r, z) = - \sum_{n=-\infty}^{\infty} \int_0^{2\pi} \int_0^{\infty} \frac{G\sigma_0 e^{-r'/r_0} r' dr' d\phi}{\sqrt{r'^2 - 2rr' \cos \phi + r^2 + (z + 2nh)^2}}, \quad (3.3)$$

with $h = \sqrt{Gm/b}$. In the following sections we examine the observational implications of the force $F = -\nabla\Phi_F$ on the disk midplane, $z = 0$.

Table 1 lists a selection of disk galaxy parameters that cover the typical values of such objects. The models G0–G8 are depicted with circles in figure 4 and are shown along with observational data (dots and triangles) from ref. [10]. The σ_0 values of the observed galaxies have been derived from Eq. (3.2) using the total baryonic mass of the galaxy, i.e. accounting for both the stars and the gas. A dot is used if the amount of the stellar mass is larger than 80% of the total mass and a triangle otherwise. Since the gas distribution does not follow the same exponential law as σ , models G0–G4 can be considered more realistic than G5–G8, which cover the region of gas-rich galaxies in the plane r_0 – σ_0 . Nevertheless, in order to investigate the various aspects of RG, Eq. (3.3) is used to explore the whole range shown in figure 4. Table 1 also includes the models M1–M3 which have a relatively higher mass and are shown with open squares in figure 4.

3.1 Rotation curves

The Newtonian and SRG forces on the midplane of a disk galaxy can be directly computed from Eqs. (3.1) and (3.3), respectively. Their values as a function of the radial distance are shown in the top panel of figure 5 for model G0. In agreement with the results of section 2.3.1, deviations appear at $r \sim h = 4.4 \text{ kpc}$; at this location F becomes larger than N , an effect that increases with radius. The dashed lines illustrate the accelerations $-Gm/r^2$ and $-Gm/rh$, assuming that the total galactic mass is concentrated in a point. Since most of the mass is enclosed within a few scale lengths, F and N converge to the corresponding asymptotic curves beyond $\sim 5r_0 = 16.5 \text{ kpc}$.

The bottom panel of figure 5 displays the orbital velocities that correspond to the Newtonian and SRG forces, respectively. At large distances v_F exhibits a flat profile which

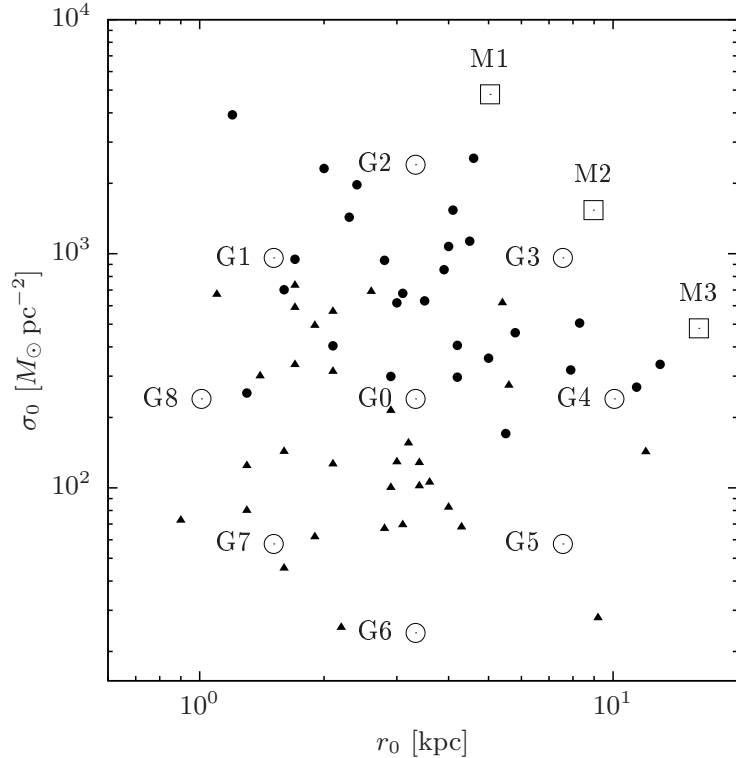


Figure 4. Typical scale lengths r_0 and surface densities σ_0 for star-dominated disk galaxies (dots) as well as disk galaxies whose gas contribution is larger than 20% (triangles) [10]. Open circles and squares denote the models listed in Table 1 and are selected such that they cover the full range of the observed parameters.

is the typical feature of most galactic rotation curves. The rotation curves for the rest of the models of Table 1 are shown in figure 6. Generally, the speed increases with radius reaching a constant value at large distances. The profiles of the high-surface-density models, G1–G3 and M1–M2, exhibit a peak after which the curves drop slightly and converge to their asymptotic limit. Conversely, models with low surface density show a rotation curve that is monotonically increasing. These features, and their dependence on the surface brightness, are in agreement with the phenomenology of spiral galaxies [11].

Moreover, the plethora of available observational data has led to empirical expressions that parametrize and fit the rotation curves of disk galaxies [12]. Comparison with such analytical formulas allows to test SRG in a general manner, avoiding the peculiarities that specific objects might have. The top panel of figure 7 plots the orbital velocities of models G0–G8 as a function of the corresponding normalized radius r/r_0 . The bottom panel shows the template rotation curves reported in ref. [12] that have been derived by fitting the data of ~ 2200 galaxies. A visual inspection suggests that the radial dependence of v_F follows these inferred expressions. The lower-mass galaxy models G6–G8 demonstrate a slowly increasing rotation curve, in agreement with the empirical rule. Similarly, the curves of the higher mass models G2–G4 reflect the initial steep increase as well as the flat profile that follows. Note that the presence of a bulge, that we neglect here, is expected to provide a stronger gradient in the inner regions. In section 4.2 below we show two specific examples of rotation curves of a high- and a low-surface-brightness galaxy, where we solve the full RG field equation rather

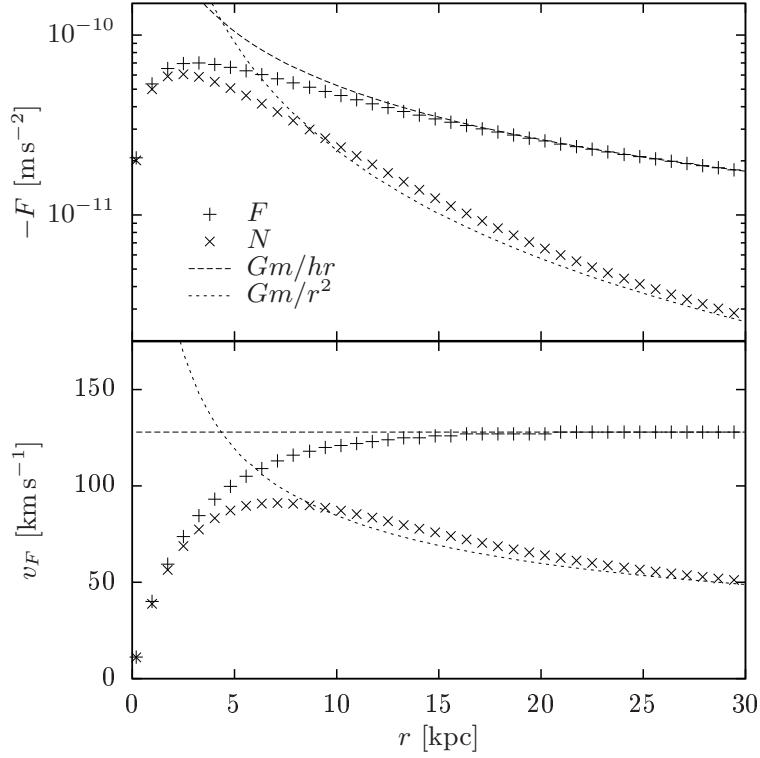


Figure 5. Top panel: radial forces for the disk galaxy G0 as given by the SRG (pluses) and Newtonian fields (crosses). The dashed lines assume that the total galactic mass is concentrated in the center. Bottom panel: orbital velocity profiles derived from the corresponding force fields. The flatness of the rotation curve becomes apparent beyond a radius comparable to a few h .

than just approximating the phenomenology with SRG.

Additional evidence comes from the centripetal acceleration and orbital velocity plotted in logarithmic scales in the top and bottom panels of figure 8 for the models G0–G8. The curves closely resemble the big collection of observations illustrated in ref. [5]. The inner regions of the high-surface-density models G2–G4 exhibit a Newtonian behavior because $r < h$ there. On the contrary, due to their small value of h , the low-surface-density models are almost entirely in the RG regime with strong deviations throughout the disk.

3.2 The baryonic Tully-Fisher relation

In the top panel of figure 9 we plot the baryonic galactic mass m as a function of the asymptotic value of the rotation curve v_f for a collection of observed galaxies (dots) [10]. The models of Table 1 (circles and squares) exactly follow the baryonic Tully-Fisher relation (solid line, Eq. 2.14), as anticipated in section 2.3.2.

Furthermore, we may define the dynamical acceleration as $a_p = v_p^2/r_p$ and the characteristic baryonic surface density as $\sigma_b = 3m/4r_p^2$, with v_p the velocity at radius r_p where the sum of the mass in stars and gas make the maximum contribution to the rotation velocity (see ref. [14]). Observationally, a_p and σ_b are closely related as shown by the data points [13] in the bottom panel of figure 9. Should the Newtonian framework be valid, we would have $a_p = G\sigma_b$, and the galaxies would follow the dotted line. However, since Eq. (2.14) gives $m = v_f^4/Gb \sim v_p^4/Gb$, SRG suggests $a_p = (4Gb/3)^{1/2}\sigma_b^{1/2}$ (solid line), a proportionality

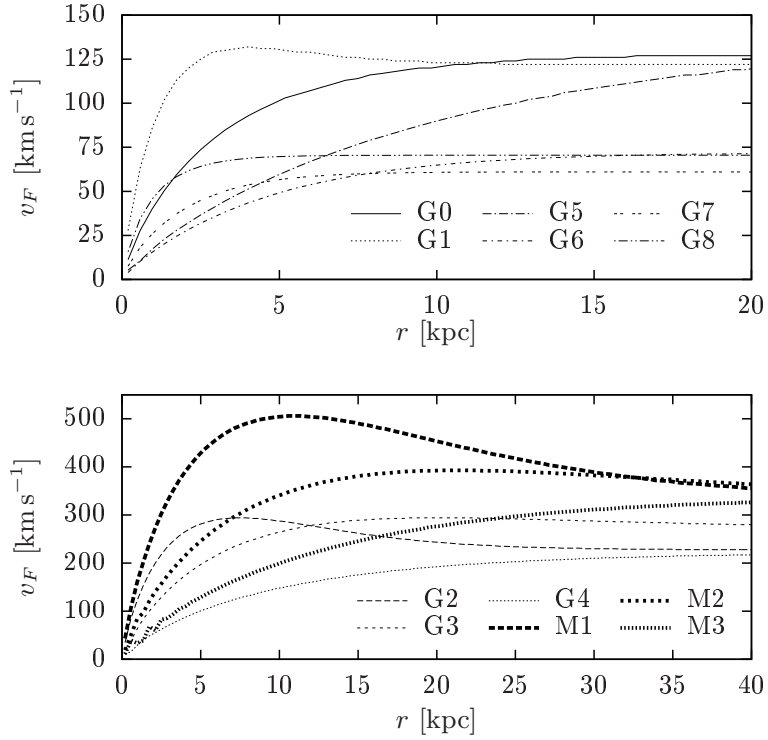


Figure 6. Rotation curves for the galaxy models listed in Table 1. All of them reach a flat profile, each one at a different radius. High-surface-density systems exhibit a peak after which the values converge to the asymptotic limit. Low-surface-density systems show a slowly-increasing velocity profile.

that is supported by observations (see also ref. [5]). Most of the models in Table 1 follow this curve (open circles and squares), with the exception of the high-surface-density models whose rotation velocity peaks in the Newtonian regime and thus they lie along the dotted line.

3.3 Mass discrepancies

Figure 10 shows the expected squared ratio between the SRG and Newtonian velocities $(v_F/v_N)^2$ for the disk galaxy models G0–G8 (solid lines). Observational data for the squared ratio between the measured and Newtonian (implied by the baryonic matter) velocities are overplotted for a sample of disk galaxies (dots) [5, 8]. We also display the curves for a selection of point masses with $m = 10^7 M_\odot, 10^8 M_\odot, \dots, 10^{12} M_\odot$ – placed in between parallel plane boundaries with $h = \sqrt{Gm/b}$ (dotted lines) – in order to capture the profiles of Eqs. (2.16), (2.17), and (2.18). The middle and bottom panels show that there is no mass discrepancy when the SRG and Newtonian accelerations are greater than $b \sim 1.2 \cdot 10^{-10} \text{ m s}^{-2}$. In contrast, the mass discrepancy increases towards the other limit, with the dependencies in good agreement with Eqs. (2.16), (2.17), and (2.18). A larger value of m relocates the radial profiles to the right (top panel), whereas the relation between mass discrepancy and force is independent of m , and thus all the dotted lines coincide (middle and bottom panels). The larger the surface density of a disk galaxy the closer it is to the point-mass curves (middle and bottom panels), with the models G1–G3 being indistinguishable from the underlying dotted

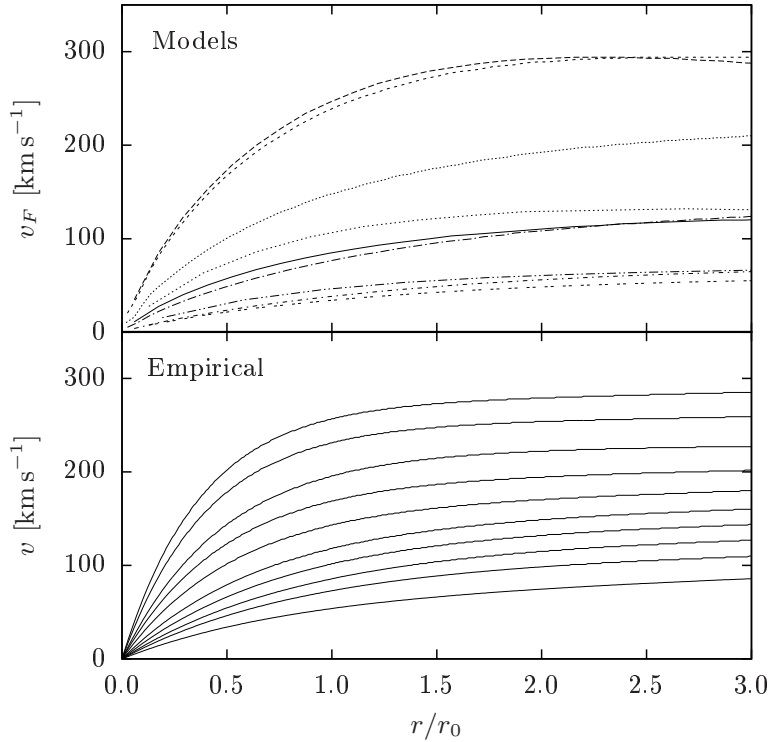


Figure 7. Rotation curves of models G0–G8 (top panel) as a function of the normalized radius r/r_0 (line types are as listed in figure 6). The template orbital velocity profiles presented in ref. [12] are displayed in the bottom panel. Both panels show a slowly-increasing curve for the low-surface-brightness galaxies. Similarities also exist for the high-surface-brightness systems, where a steep gradient at the inner regions is followed by a flat profile in the outskirts.

lines. These models fit adequately well the observed mass discrepancy data as a function of either the Newtonian or the SRG force. We note that for small σ_0 the value of b is never reached by F , as also seen in figure 8.

3.4 Velocity dispersions in the Milky Way

In SRG disk galaxies the vertical scale length h is large enough to allow the motion of stars perpendicularly to the galactic disk and to allow the presence of non-flat galactic subsystems, like the stellar halo or the system of globular clusters.

The steady-state ($\partial/\partial t = 0$) Jeans equation for the momentum is

$$\nabla \cdot (n\mathbf{w}) = n\mathbf{F}, \quad (3.4)$$

where n is the stellar number density, \mathbf{F} is the SRG acceleration, and $w_{ij} = \langle v_i v_j \rangle$ is a tensor with the brackets $\langle \rangle$ denoting averages over velocity space. In cylindrical coordinates, by assuming $\langle v_r \rangle = \langle v_z \rangle = \langle v_\phi \rangle = 0$ we obtain $w_{rr} = \langle v_r^2 \rangle = \sigma_r^2$, $w_{\phi\phi} = \langle v_\phi^2 \rangle = \sigma_\phi^2$, $w_{zz} = \langle v_z^2 \rangle = \sigma_z^2$, and $w_{rz} = \langle v_r v_z \rangle = \sigma_{rz}^2$, where σ here denotes the velocity dispersion. Under the assumption of axisymmetry, we can rewrite the radial component of the momentum equation as:

$$\frac{1}{r} \frac{\partial}{\partial r} (rn\sigma_r^2) + \frac{\partial}{\partial z} (n\sigma_{rz}^2) - \frac{n\sigma_\phi^2}{r} = nF. \quad (3.5)$$

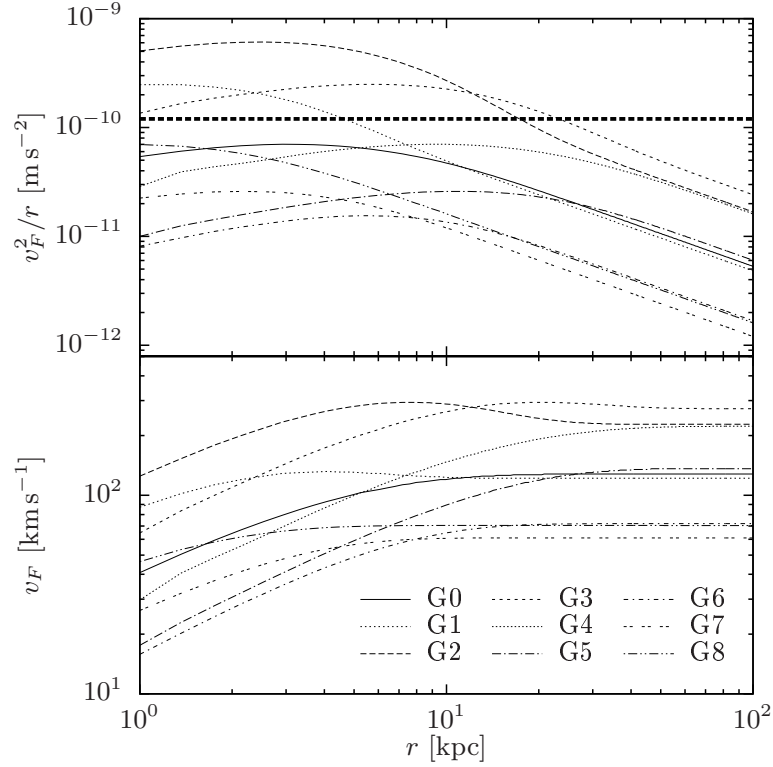


Figure 8. Centripetal acceleration (top panel) and orbital velocity (bottom panel) as a function of radius for models G0–G8. The thick horizontal dashed line denotes the value of b .

At large distances, $r \gg h$, and near $z = 0$, we may approximate the force as $F = -GM/hr = -v_f^2/r$. Then, by multiplying Eq. (3.5) by $r/n\sigma_r^2$, we obtain

$$\frac{d \ln(n\sigma_r^2)}{d \ln r} = -\frac{v_f^2}{\sigma_r^2} + \frac{\sigma_\phi^2}{\sigma_r^2} - \frac{3}{2} \pm \frac{1}{2} + \frac{\sigma_z^2}{2\sigma_r^2} \mp \frac{\sigma_z^2}{2\sigma_r^2} \equiv -p. \quad (3.6)$$

In the last expression we have taken the two extreme possibilities for $d\sigma_{rz}^2/dz$, i.e. either equal to zero (upper signs) or equal to $(\sigma_r^2 - \sigma_z^2)/r$ (lower signs), see ref. [15]. In Newtonian gravity Eq. (3.6) has an identical form, with the Newtonian velocity $v_N^2 = -rN$ in the place of v_f^2 .

We can apply Eq. (3.6) to observations of the velocity dispersion profile of the Milky Way stellar halo. A fit to these data suggests that σ_r is approximately constant at distances 20–80 kpc near the disk plane [16]. In the notation of ref. [16], σ_r is the component of the velocity dispersion along the radius in spherical coordinates, rather than in the cylindrical coordinates we use here. The two radial coordinates are clearly equal on the disk plane and thus we consider σ_r not to vary with radius. Since the anisotropy parameter β is assumed to be constant, we may also take σ_ϕ and σ_z as constants. Then Eq. (3.6) can be integrated to give

$$n(r) = Ar^{-p}, \quad (3.7)$$

where p and A are constants. In order for SRG to be consistent with observations the predicted scaling of the number density has to match the profile of the Milky Way.

Observational data indicate that, to zeroth order, v_f is roughly in the range $1.7\sigma_r$ to $2\sigma_r$ [16]. Thus the first term of p , v_f^2/σ_r^2 , takes a value between 3 and 4. Moreover, the

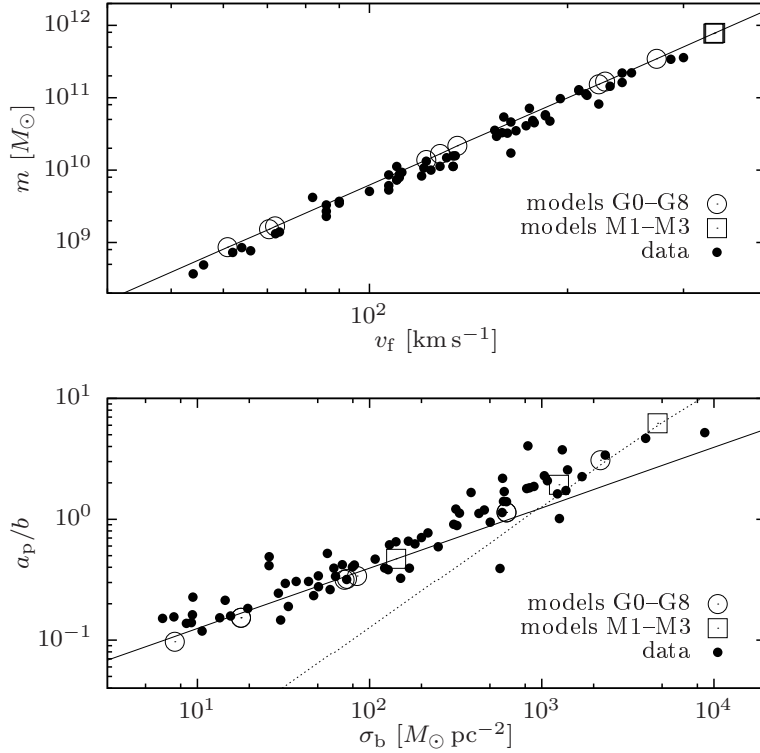


Figure 9. Top panel: the baryonic Tully-Fisher relation [7]. Eq. (2.14) is plotted with a solid line, the models of Table 1 with open circles and squares, and the observational data with dots [10]. Bottom panel: dynamical acceleration versus characteristic baryonic surface density. The Newtonian expectation (dotted line) suggests $a_p \propto \sigma_b$. However, most of the models of Table 1 (open circles and squares) as well as the observational data (dots) [13] appear to follow the proportionality $a_p \propto \sigma_b^{1/2}$ (solid line). We have multiplied the data points in the bottom panel by the factor 1.5 along the horizontal axis. This is equivalent to assuming a different stellar mass estimator and it does not affect the slope, see the discussion in ref. [13].

approximate value of the anisotropy parameter, $\beta \simeq 0.4$ [16], indicates that the tangential and radial velocity dispersion components are roughly equal; in our case this means $(\sigma_\phi^2 + \sigma_z^2)/\sigma_r^2 \simeq 1.2$. If we further consider $\sigma_\phi \simeq \sigma_z$ [15] we have $\sigma_\phi^2/\sigma_r^2 \simeq \sigma_z^2/\sigma_r^2 \simeq 0.6$. By combining the terms together we find the zeroth order approximation for p in the two limits, which is in the range 3.4 and 4.4 for the upper signs, and between 3.8 and 4.8 for the lower signs. These agree with the value $\gamma_{\text{tr}} \simeq 4$ suggested in ref. [16], which is a parameter equivalent to p . Therefore, SRG appears to be consistent with the velocity dispersions observed in the Milky Way stellar halo.

4 Solving the RG field equation

4.1 Application to a model disk galaxy

Having tested the analytical predictions of the SRG approximation, we proceed here to solve the full RG Poisson equation for a disk galaxy model from Table 1. We consider a time-independent density distribution, $\rho(r, z) = [\sigma_0/(2z_0)] \exp(-r/r_0) \exp(-z/z_0)$ (adopting the parameters of model G0), and we compute Φ by integrating Eq. (2.3) with a relaxation

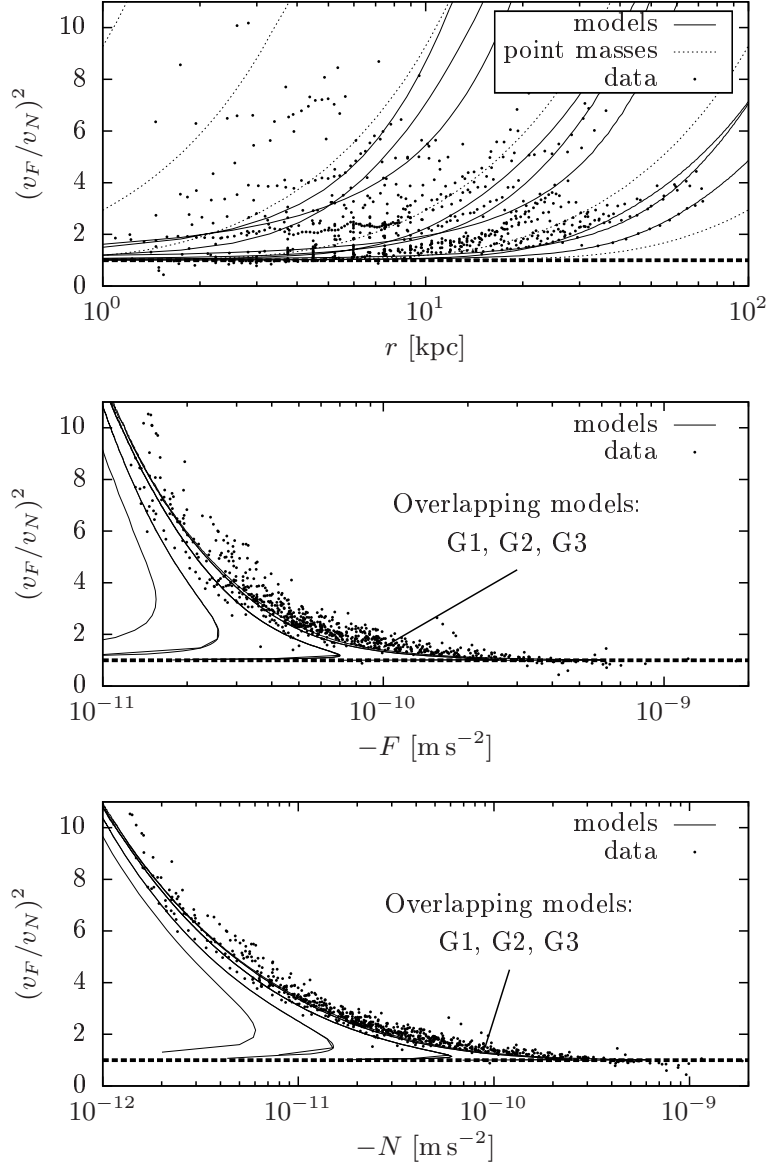


Figure 10. Discrepancies between Newtonian expectations and SRG as measured with the squared ratio of their orbital velocities, v_N and v_F , respectively. The top panel displays the radial profile, whereas the middle and bottom panels the dependence of this ratio on the SRG and Newtonian forces. The solid lines represent models G0–G8. The curves of the low-surface-density galaxies appear on the leftmost region of the middle and bottom panels, whereas they move to the right as σ_0 increases. The dotted lines represent point masses with $m = 10^7 M_\odot, 10^8 M_\odot, \dots, 10^{12} M_\odot$ (left to right in the top panel, they coincide in the middle and bottom ones). The larger the mass, the farther away the deviations become apparent. Dots are observational data from refs. [5, 8], and the thick dashed line highlights $(v_F/v_N)^2 = 1$.

numerical method. For the permittivity we assume a smooth step function from ϵ_0 to 1,

$$\epsilon(\rho) = \epsilon_0 + (1 - \epsilon_0) \frac{1}{2} \left\{ \tanh \left[\log \left(\frac{\rho}{\rho_c} \right)^q \right] + 1 \right\}, \quad (4.1)$$

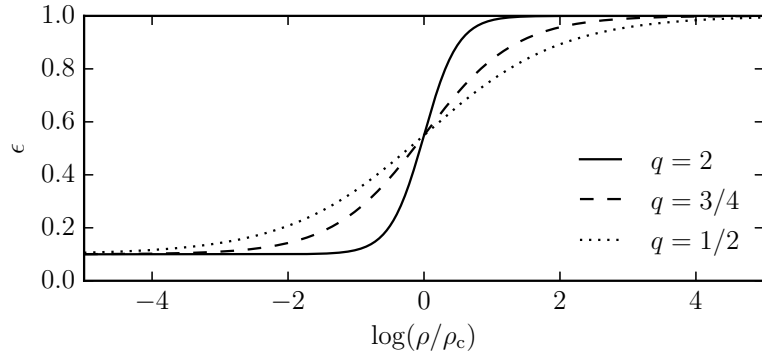


Figure 11. A simple assumption for the profile of the gravitational permittivity: Eq. (4.1) is plotted as a function of ρ/ρ_c for $\epsilon_0 = 0.1$ and three different values of q .

where q is a parameter that controls the steepness of the transition, see figure 11.

The top panel of figure 12 illustrates the gravitational field lines of model G0 in the RG (solid) and Newtonian (dashed) regimes. The refraction of the RG field is evident throughout the domain, with the effect being stronger at the outer radii. The two breaks seen along each field line, above and below the contour of ϵ (dotted line), mark the transition from $\epsilon = 1$ to ϵ_0 . For the rotation curve, the most relevant feature is the redirection of the gravitational flux that occurs at lower heights, $z \lesssim 2$ kpc, and tends to align the field lines parallelly to the disk plane.

In the bottom panels of figure 12 we plot the radial profiles of the acceleration (left) and the rotation velocity (right) along the midplane. A comparison with figure 5 confirms the validity of SRG as a powerful tool to approximate the phenomenology of disk galaxies. The slightly smaller v_f seen in figure 12 is due to the non-zero value of ϵ_0 (as compared to $\epsilon_0 = 0$ for SRG, figure 5), which results in a less efficient reorientation of the field lines along the midplane. Notably, even though the dynamical behavior in the equatorial region $r \lesssim 10$ kpc strongly deviates from the Newtonian expectation, the permittivity there is $\epsilon = 1$. This result suggests that local experiments cannot detect any discrepancies from standard gravity despite the presence of a strong background field of non-Newtonian origin.

4.2 Rotation curves of NGC1560 and NGC6946

As specific examples we model the observed rotation curves of two real disk galaxies, the high-surface-brightness NGC6946 and the low-surface-brightness NGC1560, using the surface density distributions given in ref. [5]. We complement the radial dependency with an exponential vertical profile, $\exp(-z/z_0)$, assuming $z_0 = 0.6$ kpc (NGC6946) and $z_0 = 0.2$ kpc (NGC1550) [20], and we rescale the overall ρ such that the Newtonian profiles match those shown in ref. [5] (this is equivalent to readjusting the mass-to-light ratio). For the permittivity we consider Eq. (4.1) with $q = 3/4$, $\epsilon_0 = 0.25$ and 0.20 , and critical densities $\rho_c = 10^{-24} \text{ g cm}^{-3}$ and $10^{-27} \text{ g cm}^{-3}$, respectively. The panels of figure 13 show the RG predictions for each galaxy (solid lines), which are found in agreement with the observed rotation curves (points) [17–19]. We note that the smoothness of the curve and the intensity of its features may be better captured by assuming a radially-dependent scale height. However, we refrain from improving or quantifying the fit because the assumed expression for ϵ consists

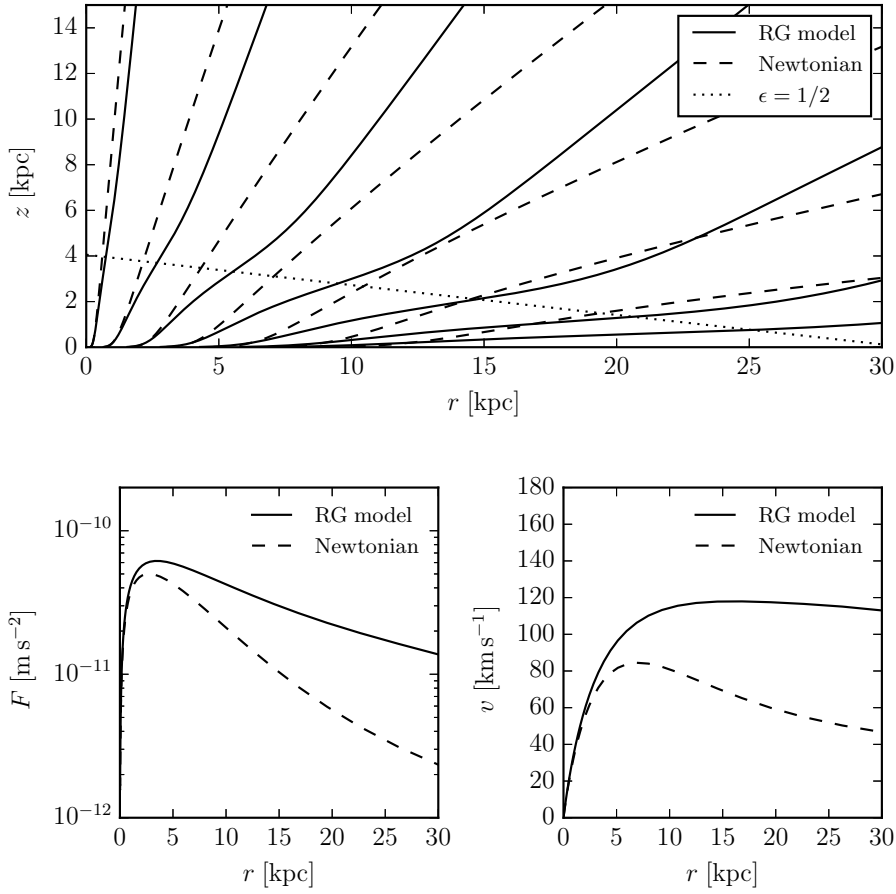


Figure 12. Top panel: Gravitational field lines (solid: RG, dashed: Newtonian gravity) for the disk galaxy model G0, as computed by Eqs. (2.3) and (4.1) for the parameters $q = 1/2$, $\epsilon_0 = 1/6$, and $\rho_c = 10^{-4}\sigma_0/2z_0$. The dotted line shows the contour $\epsilon = 1/2$. Bottom panels: Acceleration (left) and orbital velocity (right) on the midplane (compare with SRG in figure 5).

of a simplistic hypothesis, only appropriate for demonstrating the proof of concept. Further development of RG is needed for a more detailed analysis.

4.3 Intracluster gas temperature of A1991 and A1795

Finally, we apply the RG field equation to two galaxy clusters of different gas temperatures, A1991 and A1795 [21]. We set up a spherically-symmetric density distribution according to the observed gas profiles (truncated at r_{500} [21], a distance larger than the plotted range), and we add a stellar component of mass $5 \cdot 10^{10} M_\odot$ to the inner radii, $R < 10$ kpc, of A1991. The permittivity is assumed to follow Eq. (4.1), with the values here being $q = 2$, $\epsilon_0 = 0.045$ and 0.065 , respectively, and $\rho_c = 10^{-24} \text{ g cm}^{-3}$. The RG field is computed first, and then the gas temperature is calculated based on the hydrostatic equilibrium and the ideal-gas equation of state. Figure 14 shows that the emission-weighted projected temperatures that are predicted by RG (solid lines) are in agreement with *Chandra* measurements (points) [21]. The fit can be further improved by including the mass profiles of the galaxies and also by assuming more sophisticated permittivity functions beyond the speculative expression of Eq. (4.1).

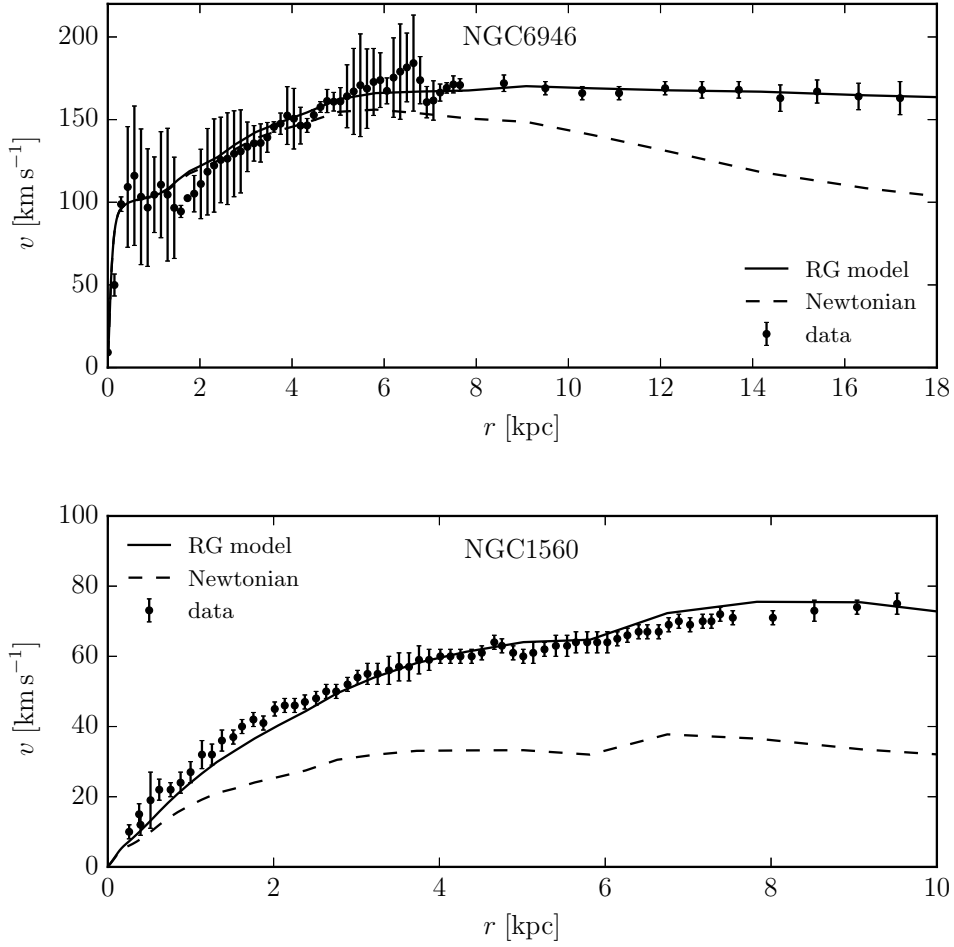


Figure 13. Rotation curves for the high-surface-brightness disk galaxy NGC6946 (top panel) and the low-surface-brightness disk galaxy NGC1560 (bottom panel). The solid and dashed lines are derived by solving the RG and Newtonian Poisson equations, respectively. The NGC6946 data points are H α and HI observations from refs. [17, 18] and the NGC1560 data are HI observations from ref. [19]. A Hubble constant $H_0 = 70 \text{ km s}^{-1} \text{ Mpc}^{-1}$ is assumed.

5 Discussion

5.1 Disk scale heights z_0 and h

Theoretical arguments as well as observational evidence suggest that the disk scale height z_0 is independent of radius [22]. A potential correlation of h with z_0 , i.e. $h \propto z_0$, would connect h with the contours of density, thus supporting the RG assumptions and the simplified equivalent framework of SRG. To investigate the hypothesis $h \propto z_0$, we show in figure 15 observational data (dots) for the scale height z_0 as a function of the maximum orbital velocity [20]. We arbitrarily choose $z_0 = 0.1h$ and overplot the corresponding points (open circles) of the models listed in Table 1. A visual inspection of this plot suggests that the assumption $h \propto z_0$ is a reasonable first approximation.

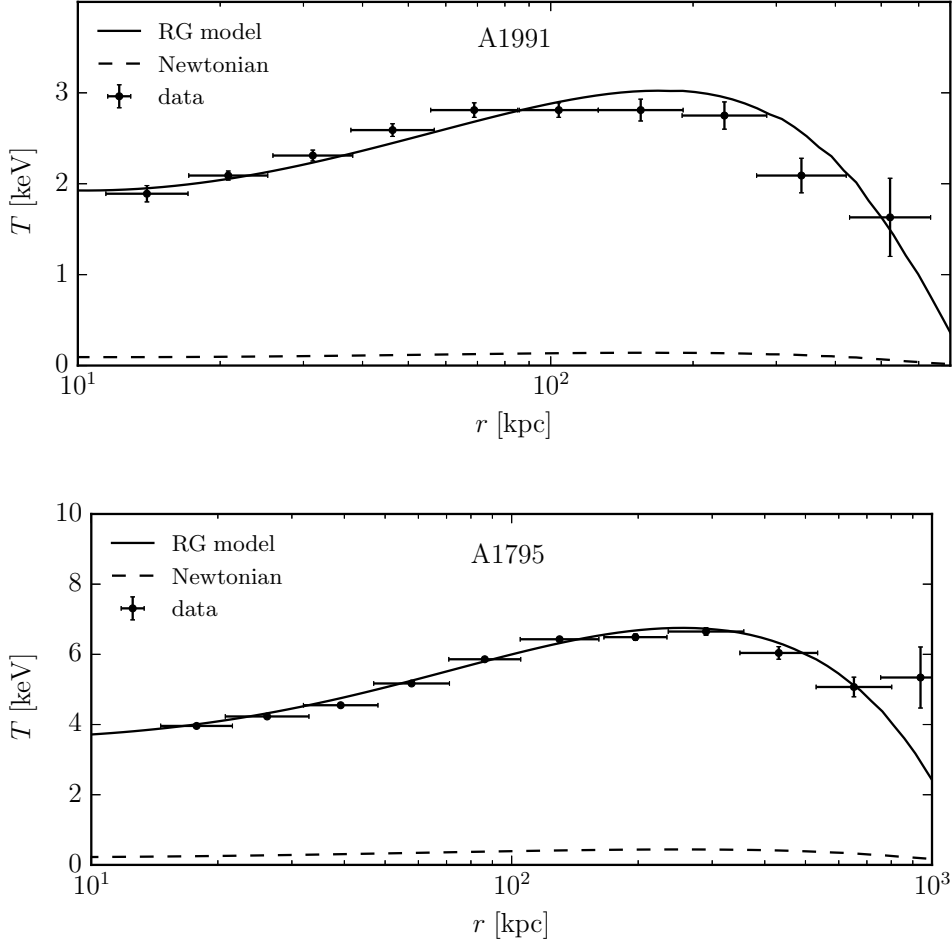


Figure 14. Emission-weighted projected temperature profiles of the intracluster gas in two galaxy clusters, A1991 (top panel) and A1795 (bottom panel). The solid lines correspond to the RG models, the dashed lines to the Newtonian expectation, and the data points are *Chandra* observations from ref. [21]. A Hubble constant $H_0 = 71 \text{ km s}^{-1} \text{ Mpc}^{-1}$ is assumed.

5.2 Relation to dark matter

In the case of disk galaxies the radial dependence of the Newtonian and RG gravitational fields at radii $r \gg h$ agree with each other if, in Newtonian gravity, we assume the presence of dark matter with mass M_{DM} :

$$\frac{G(M_{\text{DM}} + m)}{r^2} = \frac{Gm}{hr}. \quad (5.1)$$

The required amount of dark matter is thus $M_{\text{DM}} = m(r/h - 1)$ and its density profile is $\rho_{\text{DM}} = dM_{\text{DM}}/(4\pi r^2 dr) \simeq m/4\pi hr^2$. The power law behavior $\rho_{\text{DM}} \propto r^{-2}$ agrees with the NFW density profile of DM halos [23] in the region where $r \sim r_s$ (r_s is the scale radius in the notation of ref. [23]) that is inferred from the dynamics of real galaxies when interpreted with Newtonian gravity.

A similar argument can be applied to gravitational lensing. In General Relativity the deflection angle of a light ray passing at distance r from a point mass m is $\theta = 4Gm/rc^2$. To

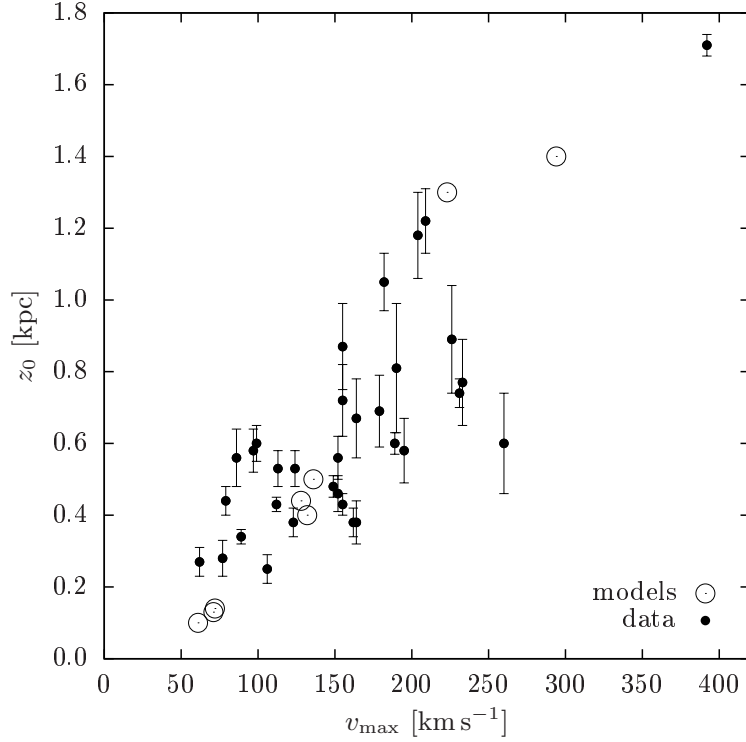


Figure 15. The scale height as a function of the maximum orbital velocity. The dots are galaxies from ref. [20] and the open circles represent the models G0–G8 assuming $z_0 = 0.1h$.

zeroth order, the modification within the RG framework is

$$\theta = \frac{4Gm}{rc^2} \frac{1}{\epsilon_0}, \quad (5.2)$$

where m is ordinary matter that, because of the permittivity of the medium, originates a gravitational field a factor $1/\epsilon_0$ stronger. We thus expect that the gas density profile in the outskirts of galaxy clusters is similar to the DM density profile inferred in Newtonian gravity, even if its density is approximately an order of magnitude smaller: this feature is indeed observed in X-ray clusters [21].

Figure 16 shows a schematic illustration of the radial dependence of the gravitational force in flat (left) and spherical systems (right), as described by Newtonian gravity in the presence of DM (top) and by the RG framework (bottom).

5.3 Relation to MOND

MOND states that below a critical acceleration (denoted with a_0) the force becomes

$$F_{\text{MOND}} = \sqrt{\frac{Gm}{r^2} a_0}. \quad (5.3)$$

By substituting a_0 with b from Eq. (2.12) we obtain:

$$F_{\text{MOND}} = \sqrt{Nb} = \sqrt{\frac{Gm}{r^2} b} = \frac{Gm}{rh}; \quad (5.4)$$

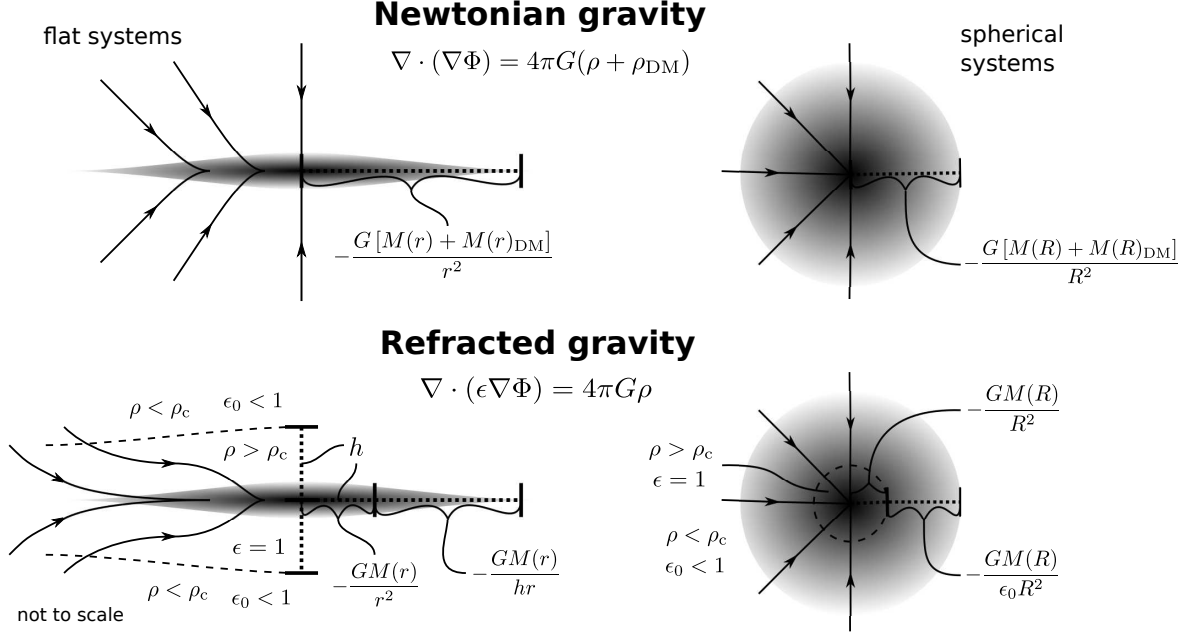


Figure 16. Schematic representation of the gravitational field lines and the approximate radial dependence of the acceleration in flat and spherical systems (top: Newtonian gravity with DM; bottom: RG). The functions $M(r)$ and $M(R)$ refer to the total enclosed mass within the cylindrical and spherical radius, respectively.

namely, it has the same profile as RG on the midplane of a flat object at distances $r \gg h$. Therefore, we expect that a significant portion of the observational successes of MOND concerning disk galaxies also belongs to RG. However, the differences between RG and MOND are fundamental.

According to the formulation of ref. [6], the Poisson equation in MOND reads

$$\nabla \cdot (\mu \nabla \Phi) = 4\pi G\rho, \quad (5.5)$$

where $\mu = \mu(|\nabla \Phi|/a_0)$. This formula is only formally similar to Eq. (2.3) of RG, because in MOND the factor μ depends on $\nabla \Phi$ itself (i.e. the field), rather than on the mass density (i.e. the source, as in the case of ϵ). Moreover, MOND exhibits non-Newtonian behavior only in regions where the local acceleration drops below the critical value $a < a_0$, but this is not the case for RG and its corresponding critical parameter ρ_c . As an example consider the midplane of disk galaxies, where even though the density is above the critical value ($\rho > \rho_c$ and thus $\epsilon = 1$) RG predicts strong deviations from Newtonian gravity (see figure 12). This is due to the redirection of the gravitational flux that occurs non-locally and provides a stronger background field. Nonetheless, since $\epsilon = 1$ there, local experiments would be in full agreement with standard gravity.

We further highlight the fundamental differences by comparing the predictions of RG and MOND for spherical and flat sources. First, consider a point mass m within a background density $\rho > \rho_c$. RG gives the exact Newtonian behavior for any radius R , i.e. $F = N \propto R^{-2}$. Even though F_{MOND} follows this profile close to the source, the radial dependence becomes $F_{\text{MOND}} \propto R^{-1}$ at large distances where the acceleration falls below a_0 . Consider now the case where the point source is in empty space, for which MOND exhibits the same phenomenology

as the example above. In RG the force now is $F = N/\epsilon_0 \propto R^{-2}$ (for any radius), which implies that a gravitational source surrounded by empty space appears to be more massive due to the permittivity of vacuum $\epsilon_0 < 1$, but the power law remains Newtonian. In principle, RG and MOND can be distinguished observationally by measuring the field in spherical systems, such as globular or galaxy clusters, at large distances where the background density and/or the acceleration drop below the critical value.

On the other hand, both MOND and RG predict almost the same radial dependence on the midplane of flat objects: the gravitational field is proportional to r^{-2} at inner radii and to r^{-1} in the outskirts. However, above and below the disk the predictions can be different. Depending on the height and how the field lines are refracted (location and shape of ρ_c), RG is expected to give a Newtonian vertical field within $z = \pm h$. In contrast MOND suggests a strong acceleration, which is always in the MONDian regime far away from the source. A detailed analysis of the rotation curves and the stellar velocity dispersion profiles of disk galaxies from the DiskMass Survey [24] has recently shown that MOND requires a relation between scale lengths and scale heights substantially flatter than observed: in MOND, once the mass-to-light ratio is set by the rotation curve, the vertical component of the gravitational force is larger than in Newtonian gravity. This effect propagates into the thickness of a disk galaxy in MOND: the thickness should be a factor of 2 smaller than the thickness estimated from the observation of edge-on galaxies [24]. We expect that RG might not suffer from this problem.

Similarly, in some dwarf spheroidal galaxies MOND requires radial velocity dispersion profiles larger than observed [25, 26], a fact that might again be naturally solved by RG. A detailed analysis of all these topics within the RG framework is clearly needed.

6 Other applications

The following subsections discuss the relevance of the RG framework to other systems that exhibit mass discrepancies. We plan to investigate quantitatively the predictions of RG for such systems in future work.

6.1 Globular clusters

Since globular clusters are spherically symmetric systems, RG does not predict any redirection of the gravitational field lines. In addition, as long as the background density is larger than ρ_c , no substantial deviations from Newtonian dynamics are expected. This behavior is compatible with the numerous observations that confirm the validity of Newtonian gravity, even though the acceleration over a part of the globular cluster volumes is below a_0 [e.g., 27–32]. However, there are systems that suggest a non-Newtonian behavior at large distances [e.g., 33–35], and these could possibly be addressed with a change in ϵ . By combining measurements of the background density profile in Newtonian and non-Newtonian clusters we can in principle constrain the critical values of the density ρ_c and the permittivity ϵ .

6.2 Dwarf spheroidal galaxies

Dwarf spheroidal galaxies, whose baryonic masses are comparable to the mass of globular clusters but have a much lower surface brightness, show evidence of large mass discrepancies [e.g., 36–38]. In RG this mass discrepancy is a consequence of the dwarf galaxy shapes, which is significantly flatter than in globular clusters [e.g., 39, 40]. In particular, we expect a departure from Newtonian gravity due to the redirection of the gravitational flux along the

dwarf midplane. Because of the low surface brightness of dwarfs, RG suggests that the non-Newtonian features are even stronger than in disk galaxies, as it can be seen from figure 8 and the corresponding discussion: the value of h is relatively smaller, and thus a non-Newtonian behavior is expected almost within the entire volume of the dwarf ($r > h$).

6.3 Elliptical galaxies

It has recently been suggested that the amount of extra mass required to explain the dynamics of elliptical galaxies depends on the ellipticity of their shape [41]. Specifically, flatter elliptical galaxies seem to show larger mass discrepancies than more roundish ones. In the same context as globular clusters and dwarf spheroidal galaxies, this feature arises naturally within the framework of RG: the flatter the shape of a galaxy is, the stronger the field-redirection effect becomes. Moreover, in RG the Tully-Fisher relation (Eq. 2.14) can be derived only for the case of disk galaxies, but it is not expected to hold for galaxies without a flat morphology. This conclusion seems to be supported by a recent study [42] which suggests that disk-like galaxies tightly follow the Tully-Fisher relation, whereas those that scatter off are morphologically different.

6.4 Disk galaxies

Since ordinary matter is the only source of gravity within the framework of RG, the correlation between the features of the rotation curves and the features of the surface brightness distribution, as observed in several disk galaxies (the so-called “Renzo’s rule”) [43, 44], is clearly expected. Furthermore, the observed scaling relation $dv/dr \propto \sqrt{\rho_0}$ (where ρ_0 is the central density), holding in the inner regions of disk galaxies [45], also naturally arises in RG because its gravity intensity reduces to the Newtonian intensity close to the galactic center.

6.5 Galaxy groups and clusters

In RG the evaluation of the gravitational interactions between galaxies, that occur in groups and clusters, is complicated by the redirection of the lines of the gravitational field originated by each galaxy faraway from the galaxy main body, namely beyond the surface of constant critical density ρ_c . As shown in the example of a disk galaxy in figure 12, the shape of the iso-contour of ρ_c determines the refraction angle and thus the dependence of the gravitational force on the radial distance r from the galaxy center.

If we overlook this complication and simply assume that the galactic gravitational field of each galaxy decreases with r^{-1} at large radii, the net modification of RG, compared to standard gravity, is to increase the field intensity by a factor $1/\epsilon_0$ due the gravitational permittivity of low-density regions (see section 2.2.3). Therefore, the extension of the baryonic Tully-Fisher relation (Eq. 2.14) to galaxy groups and clusters becomes

$$v_f^4 = Gbf \frac{km}{\epsilon_0}, \quad (6.1)$$

where k is the number of galaxies (each with mass m) in the system and $f < 1$ is a geometric factor that accounts for the fact that, due to the anisotropic RG field geometry of disk galaxies, only a fraction of the k members will cross the plane of a given disk galaxy where the force is $\propto r^{-1}$.

Figure 17 shows Eq. (6.1) for $f/\epsilon_0 = 1.3$ (dashed line), along with data points for galaxy groups and clusters [46, 47]. The observed baryonic Tully-Fisher relation for such systems

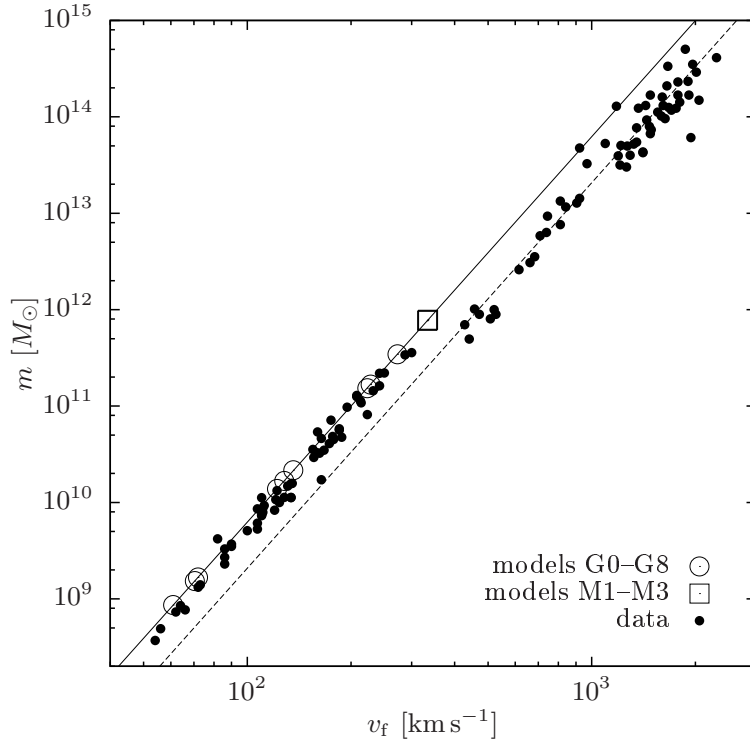


Figure 17. The baryonic Tully-Fisher relation – same as the top panel of figure 9, but at larger mass and velocity scales in order to include galaxy groups and galaxy clusters. Equation (2.14) is plotted with a solid line and Eq. (6.1) is plotted with a dashed line for $f/\epsilon_0 = 1.3$. The additional observational data for groups and clusters that appear in the upper right part of the plot (dots) are taken from refs. [46, 47].

shows a smaller normalization than the relation for galaxies, but its slope remains unaltered in agreement with the approximate RG expectation. In fact, this qualitative analysis suggests a procedure to estimate the critical value of the density and the permittivity ϵ_0 . In addition, Eq. (6.1) implicitly assumes that the intracluster medium (ICM) has a density below the critical value, as it was also indicated by the fits in section 4.3. This property could be used to set a lower limit to the value of ρ_c .

7 Conclusion

In this paper we investigate an alternative approach to describe the dynamics of galaxies and larger cosmic structures without requiring the existence of dark matter. Motivated by the Poisson equation of electrodynamics in matter, we propose that the mass discrepancies originate from a gravitational permittivity that depends on the local mass density and effectively refracts the field lines. This effect can make the gravitational field significantly stronger than the Newtonian one, with the expected deviations depending on both the total mass and its distribution.

We show that this framework can successfully describe several observational features of disk galaxies, such as the rotation curves and the baryonic Tully-Fisher relation, as well as the basic phenomenology of galaxy groups and clusters. We also discuss the specific features of

refracted gravity that might explain why systems of similar luminous mass have significantly different dynamical properties, for example globular clusters and dwarf galaxies, or disk and elliptical galaxies.

It thus appears that refracted gravity might provide a promising approach to describe the phenomenology of cosmic structures. We conclude that it is worth developing the theoretical foundation of this model in detail and investigating its observational expectations more rigorously. This future work will assess whether refracted gravity can ultimately be considered a valid theory or suffers from unsolvable failures.

Acknowledgments

We are grateful to Stacy McGaugh for providing us with the data points that appear in several of our figures, as well as for his useful comments. We would also like to thank Garry Angus and Justin Khoury for fruitful discussions on several aspects of this work. AD acknowledges partial support from the INFN grant InDark, the grant Progetti di Ateneo TO Call 2012 0011 ‘Marco Polo’ of the University of Torino and the grant PRIN 2012 “Fisica Astroparticellare Teorica” of the Italian Ministry of University and Research.

References

- [1] A. Del Popolo, *Nonbaryonic Dark Matter in Cosmology*, *International Journal of Modern Physics D* **23** (Mar., 2014) 30005, [[arXiv:1305.0456](#)].
- [2] M. Milgrom, *A modification of the Newtonian dynamics as a possible alternative to the hidden mass hypothesis*, *ApJ* **270** (July, 1983) 365–370.
- [3] M. Milgrom, *A modification of the Newtonian dynamics - Implications for galaxies*, *ApJ* **270** (July, 1983) 371–389.
- [4] M. Milgrom, *A Modification of the Newtonian Dynamics - Implications for Galaxy Systems*, *ApJ* **270** (July, 1983) 384.
- [5] B. Famaey and S. S. McGaugh, *Modified Newtonian Dynamics (MOND): Observational Phenomenology and Relativistic Extensions*, *Living Reviews in Relativity* **15** (Sept., 2012) 10, [[arXiv:1112.3960](#)].
- [6] J. Bekenstein and M. Milgrom, *Does the missing mass problem signal the breakdown of Newtonian gravity?*, *ApJ* **286** (Nov., 1984) 7–14.
- [7] R. B. Tully and J. R. Fisher, *A new method of determining distances to galaxies*, *A&A* **54** (Feb., 1977) 661–673.
- [8] S. S. McGaugh, *The Mass Discrepancy-Acceleration Relation: Disk Mass and the Dark Matter Distribution*, *ApJ* **609** (July, 2004) 652–666, [[astro-ph/0](#)].
- [9] K. C. Freeman, *On the Disks of Spiral and so Galaxies*, *ApJ* **160** (June, 1970) 811.
- [10] S. S. McGaugh, *The Baryonic Tully-Fisher Relation of Galaxies with Extended Rotation Curves and the Stellar Mass of Rotating Galaxies*, *ApJ* **632** (Oct., 2005) 859–871, [[astro-ph/0](#)].
- [11] M. Persic, P. Salucci, and F. Stel, *The universal rotation curve of spiral galaxies - I. The dark matter connection*, *MNRAS* **281** (July, 1996) 27–47, [[astro-ph/9506004](#)].
- [12] B. Catinella, R. Giovanelli, and M. P. Haynes, *Template Rotation Curves for Disk Galaxies*, *ApJ* **640** (Apr., 2006) 751–761, [[astro-ph/0](#)].
- [13] S. McGaugh, *Baryons and Their Halos*, in *American Institute of Physics Conference Series* (V. P. Debattista and C. C. Popescu, eds.), vol. 1240 of *American Institute of Physics Conference Series*, pp. 13–16, June, 2010. [arXiv:0912.3943](#).

- [14] S. S. McGaugh, *Balance of Dark and Luminous Mass in Rotating Galaxies*, *Physical Review Letters* **95** (Oct., 2005) 171302, [[astro-ph/0](#)].
- [15] J. Binney and S. Tremaine, *Galactic Dynamics: Second Edition*. Princeton University Press, 2008.
- [16] O. Y. Gnedin, W. R. Brown, M. J. Geller, and S. J. Kenyon, *The Mass Profile of the Galaxy to 80 kpc*, *ApJL* **720** (Sept., 2010) L108–L112, [[arXiv:1005.2619](#)].
- [17] O. Daigle, C. Carignan, P. Amram, O. Hernandez, L. Chemin, C. Balkowski, and R. Kennicutt, *H α kinematics of the SINGS nearby galaxies survey - I*, *MNRAS* **367** (Apr., 2006) 469–512, [[astro-ph/0601376](#)].
- [18] R. Boomsma, T. A. Oosterloo, F. Fraternali, J. M. van der Hulst, and R. Sancisi, *HI holes and high-velocity clouds in the spiral galaxy NGC 6946*, *A&A* **490** (Nov., 2008) 555–570, [[arXiv:0807.3339](#)].
- [19] G. Gentile, M. Baes, B. Famaey, and K. van Acoleyen, *Mass models from high-resolution HI data of the dwarf galaxy NGC 1560*, *MNRAS* **406** (Aug., 2010) 2493–2503, [[arXiv:1004.3421](#)].
- [20] M. Kregel, P. C. van der Kruit, and R. de Grijs, *Flattening and truncation of stellar discs in edge-on spiral galaxies*, *MNRAS* **334** (Aug., 2002) 646–668, [[astro-ph/0](#)].
- [21] A. Vikhlinin, A. Kravtsov, W. Forman, C. Jones, M. Markevitch, S. S. Murray, and L. Van Speybroeck, *Chandra Sample of Nearby Relaxed Galaxy Clusters: Mass, Gas Fraction, and Mass-Temperature Relation*, *ApJ* **640** (Apr., 2006) 691–709, [[astro-ph/0507092](#)].
- [22] P. C. van der Kruit and L. Searle, *Surface photometry of edge-on spiral galaxies. I - A model for the three-dimensional distribution of light in galactic disks*, *A&A* **95** (Feb., 1981) 105–115.
- [23] J. F. Navarro, C. S. Frenk, and S. D. M. White, *A Universal Density Profile from Hierarchical Clustering*, *ApJ* **490** (Dec., 1997) 493–508, [[astro-ph/9611107](#)].
- [24] G. W. Angus, G. Gentile, R. Swaters, B. Famaey, A. Diaferio, S. S. McGaugh, and K. J. v. d. Heyden, *Mass models of disc galaxies from the DiskMass Survey in modified Newtonian dynamics*, *MNRAS* **451** (Aug., 2015) 3551–3580, [[arXiv:1505.05522](#)].
- [25] G. W. Angus, *Dwarf spheroidals in MOND*, *MNRAS* **387** (July, 2008) 1481–1488, [[arXiv:0804.3812](#)].
- [26] G. W. Angus, G. Gentile, A. Diaferio, B. Famaey, and K. J. van der Heyden, *N-body simulations of the Carina dSph in MOND*, *MNRAS* **440** (May, 2014) 746–761, [[arXiv:1403.4119](#)].
- [27] H. Baumgardt, E. K. Grebel, and P. Kroupa, *Using distant globular clusters as a test for gravitational theories*, *MNRAS* **359** (May, 2005) L1–L4, [[astro-ph/0](#)].
- [28] H. Baumgardt, P. Côté, M. Hilker, et al., *The velocity dispersion and mass-to-light ratio of the remote halo globular cluster NGC 2419*, *MNRAS* **396** (July, 2009) 2051–2060, [[arXiv:0904.3329](#)].
- [29] K. Jordi, E. K. Grebel, M. Hilker, et al., *Testing Fundamental Physics with Distant Star Clusters: Analysis of Observational Data on Palomar 14*, *AJ* **137** (June, 2009) 4586–4596, [[arXiv:0903.4448](#)].
- [30] R. Ibata, A. Sollima, C. Nipoti, et al., *The Globular Cluster NGC 2419: A Crucible for Theories of Gravity*, *ApJ* **738** (Sept., 2011) 186, [[arXiv:1106.4909](#)].
- [31] R. Ibata, A. Sollima, C. Nipoti, et al., *Polytropic Model Fits to the Globular Cluster NGC 2419 in Modified Newtonian Dynamics*, *ApJ* **743** (Dec., 2011) 43, [[arXiv:1110.3892](#)].
- [32] M. J. Frank, M. Hilker, H. Baumgardt, et al., *The velocity dispersion and mass function of the outer halo globular cluster Palomar 4*, *MNRAS* **423** (July, 2012) 2917–2932, [[arXiv:1205.2693](#)].

- [33] R. Scarpa, G. Marconi, R. Gilmozzi, and G. Carraro, *Using globular clusters to test gravity in the weak acceleration regime: NGC 7099*, *A&A* **462** (Jan., 2007) L9–L12, [[astro-ph/0611504](#)].
- [34] R. Scarpa and R. Falomo, *Testing Newtonian gravity in the low acceleration regime with globular clusters: the case of ω Centauri revisited*, *A&A* **523** (Nov., 2010) A43, [[arXiv:1006.4577](#)].
- [35] R. Scarpa, G. Marconi, G. Carraro, R. Falomo, and S. Villanova, *Testing Newtonian gravity with distant globular clusters: NGC 1851 and NGC 1904*, *A&A* **525** (Jan., 2011) A148, [[arXiv:1008.3526](#)].
- [36] M. G. Walker, M. Mateo, E. W. Olszewski, et al., *Velocity Dispersion Profiles of Seven Dwarf Spheroidal Galaxies*, *ApJL* **667** (Sept., 2007) L53–L56, [[arXiv:0708.0010](#)].
- [37] L. E. Strigari, J. S. Bullock, M. Kaplinghat, et al., *A common mass scale for satellite galaxies of the Milky Way*, *Nature* **454** (Aug., 2008) 1096–1097, [[arXiv:0808.3772](#)].
- [38] L. E. Strigari, S. M. Koushiappas, J. S. Bullock, et al., *The Most Dark-Matter-dominated Galaxies: Predicted Gamma-Ray Signals from the Faintest Milky Way Dwarfs*, *ApJ* **678** (May, 2008) 614–620, [[arXiv:0709.1510](#)].
- [39] S. van den Bergh, *The luminosity-diameter relations for globular clusters and dwarf spheroidal galaxies*, *MNRAS* **390** (Oct., 2008) L51–L53, [[arXiv:0807.2798](#)].
- [40] S. van den Bergh, *Globular clusters and dwarf spheroidal galaxies*, *MNRAS* **385** (Mar., 2008) L20–L22, [[arXiv:0711.4795](#)].
- [41] A. Deur, *A relation between the dark mass of elliptical galaxies and their shape*, *MNRAS* **438** (Feb., 2014) 1535–1551, [[arXiv:1304.6932](#)].
- [42] R. C. Simons, S. A. Kassin, B. J. Weiner, T. M. Heckman, J. C. Lee, J. M. Lotz, M. Peth, and K. Tchernyshyov, *A transition mass in the local Tully-Fisher relation*, *MNRAS* **452** (Sept., 2015) 986–997, [[arXiv:1506.04144](#)].
- [43] R. Sancisi, *The visible matter – dark matter coupling*, in *Dark Matter in Galaxies* (S. Ryder, D. Pisano, M. Walker, and K. Freeman, eds.), vol. 220 of *IAU Symposium*, p. 233, July, 2004. [astro-ph/0](#).
- [44] R. A. Swaters, R. Sancisi, J. M. van der Hulst, and T. S. van Albada, *The link between the baryonic mass distribution and the rotation curve shape*, *MNRAS* **425** (Sept., 2012) 2299–2308, [[arXiv:1207.2729](#)].
- [45] F. Lelli, F. Fraternali, and M. Verheijen, *A scaling relation for disc galaxies: circular-velocity gradient versus central surface brightness*, *MNRAS* **433** (June, 2013) L30–L34, [[arXiv:1304.4250](#)].
- [46] R. H. Sanders, *Clusters of galaxies with modified Newtonian dynamics*, *MNRAS* **342** (July, 2003) 901–908, [[astro-ph/0212293](#)].
- [47] S. S. McGaugh, *A tale of two paradigms: the mutual incommensurability of Λ CDM and MOND*, *Canadian Journal of Physics* **93** (Feb., 2015) 250–259, [[arXiv:1404.7525](#)].